



## Bridging energy bands to the crystalline and amorphous states of Si QDs

Mariotti, D., Alessi, B., Chiranjeevi, M., Macias-Montero, M., Svrcek, V., & Maguire, P. (2020). Bridging energy bands to the crystalline and amorphous states of Si QDs. *Faraday Discussions*, 222, 390-404.  
<https://doi.org/10.1039/C9FD00103D>

[Link to publication record in Ulster University Research Portal](#)

**Published in:**  
Faraday Discussions

**Publication Status:**  
Published (in print/issue): 19/06/2020

**DOI:**  
[10.1039/C9FD00103D](https://doi.org/10.1039/C9FD00103D)

**Document Version**  
Author Accepted version

**Document Licence:**  
CC BY

### General rights

The copyright and moral rights to the output are retained by the output author(s), unless otherwise stated by the document licence.

Unless otherwise stated, users are permitted to download a copy of the output for personal study or non-commercial research and are permitted to freely distribute the URL of the output. They are not permitted to alter, reproduce, distribute or make any commercial use of the output without obtaining the permission of the author(s).

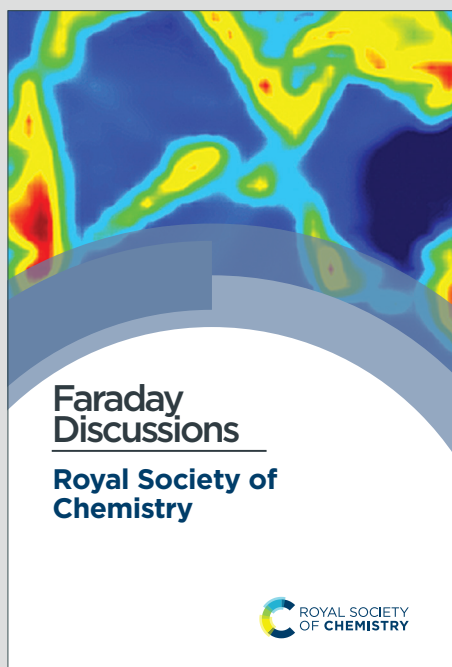
If the document is licenced under Creative Commons, the rights of users of the documents can be found at <https://creativecommons.org/share-your-work/licenses/>.

### Take down policy

The Research Portal is Ulster University's institutional repository that provides access to Ulster's research outputs. Every effort has been made to ensure that content in the Research Portal does not infringe any person's rights, or applicable UK laws. If you discover content in the Research Portal that you believe breaches copyright or violates any law, please contact [pure-support@ulster.ac.uk](mailto:pure-support@ulster.ac.uk)

# Faraday Discussions

Accepted Manuscript



This is an Accepted Manuscript, which has been through the Royal Society of Chemistry peer review process and has been accepted for publication.

Accepted Manuscripts are published online shortly after acceptance, before technical editing, formatting and proof reading. Using this free service, authors can make their results available to the community, in citable form, before we publish the edited article. We will replace this Accepted Manuscript with the edited and formatted Advance Article as soon as it is available.

You can find more information about Accepted Manuscripts in the [Information for Authors](#).

Please note that technical editing may introduce minor changes to the text and/or graphics, which may alter content. The journal's standard [Terms & Conditions](#) and the [Ethical guidelines](#) still apply. In no event shall the Royal Society of Chemistry be held responsible for any errors or omissions in this Accepted Manuscript or any consequences arising from the use of any information it contains.

This article can be cited before page numbers have been issued, to do this please use: D. Mariotti, B. Alessi, M. Chiranjeevi, M. Macias-Montero, V. Svrcek and P. Maguire, *Faraday Discuss.*, 2020, DOI: 10.1039/C9FD00103D.

# Bridging energy bands to the crystalline and amorphous states of Si QDs

*Bruno Alessi<sup>1\*</sup>, Manuel Macias-Montero<sup>2</sup>, Chiranjeevi Maddi<sup>1</sup>, Paul Maguire<sup>1</sup>, Vladimir Svrcek<sup>3</sup>, Davide Mariotti<sup>1</sup>*

<sup>1</sup>Nanotechnology and Integrated Bio-Engineering Centre (NIBEC), Ulster University, Newtownabbey BT37 0QB, United Kingdom

<sup>2</sup>Laser Processing Group, Institute of Optics (CSIC), Serrano 121, 28006 Madrid, Spain

<sup>3</sup>Research Center for Photovoltaics National Institute of Advanced Industrial Science and Technology (AIST) Central 2, Umezono 1-1-1, Tsukuba, 305-8568, Japan

\*e-mail: alessi-b@ulster.ac.uk

## Keywords

Silicon quantum dots, atmospheric-pressure plasmas, valence electron energy diagram, crystallization process

## Abstract

The relationship between crystallization process and opto-electronic properties of silicon quantum dots (Si QDs) synthesized by atmospheric pressure plasmas (APPs) is studied in this work. The synthesis of Si QDs is carried out flowing silane as gas precursor in a plasma confined to a submillimeter space. Experimental conditions are adjusted to propitiate the crystallization of the Si QDs and produce QDs with both an amorphous and a crystalline character. In all the cases, Si QDs present a well-defined particle mean size in the range of 1.5-5.5 nm. Si QDs present optical bandgaps between 2.3 eV and 2.5 eV, which are affected by quantum confinement. Plasma parameters evaluated using optical emission spectroscopy are then used as inputs for a collisional plasma model, whose calculations yield the surface temperature of the Si QDs within the plasma, justifying the crystallization behavior for certain experimental conditions. We measure the ultraviolet-visible optical properties and electronic properties through various techniques, build an energy level diagram for the valence electrons region as a function of the crystallinity of the QDs and finally discuss the integration of these as active layers of all-inorganic solar cells.



## 28 1. Introduction

View Article Online

DOI: 10.1039/C9FD00103D

29  
30 The unique properties of silicon quantum dots (QDs) have attracted great attention in numerous  
31 fields of science such as photonics, photovoltaics, electronics or biomedicine [1-5] for the unique  
32 interplay between quantum effects, surface states and direct/indirect transition dynamics and their  
33 biocompatibility [6-8]. Over the last decade, the focus has been on crystalline Si QDs [9-14], and  
34 the efforts made on the study of amorphous Si QDs have been very limited [15-18] due to the  
35 difficulty of preserving the individual character of the QDs. Nonetheless, both phases present  
36 distinguished and remarkable features. Amorphous silicon thin films often offer better transport  
37 properties due to enhanced structural disorder preventing radiative recombination [19] and  
38 tunability of their optical absorption edge by controlling hydrogen content [16]. At the nanoscale,  
39 QDs can provide added functionalities not available from bulk silicon for amorphous and  
40 crystalline Si, in combination with other nanoscale properties (surface-to-volume ratio, surface  
41 chemistries, etc.). The synthesis of Si QDs by low-pressure plasma has been the focus of extended  
42 research work that has revealed the benefits of plasma processes for nanomaterials synthesis [20-  
43 23]. Non-thermal plasmas at atmospheric pressure offer beneficial and complementary features  
44 but have received limited attention.

45 Atmospheric pressure plasmas (APPs) present great versatility for the production and  
46 treatment of nanomaterials [24, 25] for they allow flexible design and easy integrability. Also, at  
47 this pressure, ion collisions with the surface of nanoparticles are responsible for particle heating  
48 above the background gas temperature, allowing a controlled crystallization [14] by carefully  
49 tuning the synthesis conditions. We have previously studied the synthesis and materials properties  
50 of crystalline and amorphous silicon QDs, separately, by atmospheric pressure plasmas (APPs)  
51 [16, 26, 27]. Our approach produced Si QDs with well-defined particle size and with observable  
52 quantum confinement effects.

53 Herein, we present an experimental and theoretical investigation of the Si QDs phase transition  
54 in APPs, comparing the plasma conditions leading to or preventing crystallization.

55 We then perform various measurements on selected samples to assess the energy band diagrams  
56 and derive the relationships between structural features and opto-electronic properties in function  
57 of synthesis conditions. In this context we use different measurements techniques to build an  
58 energy level diagram of near-gap electron states, and critically compare methods and results. This  
59 approach is important for implementing nanomaterials in real world applications.

60 Finally, we test the applicability of our Si QDs integrating them as active layers in all-inorganic  
61 solar cells. While these devices still present very low efficiencies, here we demonstrate the  
62 viability of APP processes to be used in the manufacturing of next generation photovoltaics.

63



## 64 2. Experimental details

65 The plasma reactor used for the synthesis of Si QDs operates in a parallel electrode  
66 configuration at atmospheric pressure (760 Torr). A schematic diagram of the system is depicted  
67 in Figure S1 of supporting information. The plasma is generated inside a rectangular glass tube  
68 with a 0.5 mm gap and 0.3 mm of wall thickness. Radio frequency (RF) power at 13.56 MHz and  
69 120 W is applied through a matching unit and to two rectangular copper electrodes with a section  
70 of 20 mm x 5 mm.

71 Argon and hydrogen are supplied as background gases, while silane ( $\text{SiH}_4$ ) is used as Si  
72 precursor varying its concentration between 50 ppm and 200 ppm. The flows of Ar and  $\text{H}_2$  are set  
73 to 810-840 sccm and 150 sccm respectively, in order to keep concentrations of 99.7% and 0.3%  
74 approximately at a fixed total flow of 1 sLm. The plasma setup is accessorized with a two-axis  
75 stage and it is possible to directly deposit Si QDs on a substrate and form homogeneous films  
76 [26]. The plasma conditions are characterized using optical emission spectroscopy. The  
77 equipment used to acquire the emission spectra is an Ocean Optics HR4000CG UV-NIR  
78 spectrometer (range 194-1122 nm) coupled with a 50  $\mu\text{m}$  optic fiber. These measurements are  
79 carried out locating one end of the optic fiber perpendicular to the plasma 10 mm away.

80 Silicon QDs are characterized using transmission electron microscopy (TEM) with a JEOL  
81 JEM-2100F microscope. The TEM analysis includes bright-field imaging to observe the  
82 morphology of the QDs and selected area electron diffraction (SAED) to characterize their  
83 crystallinity. For TEM, the QDs are collected directly in vials containing ethanol and then drop  
84 casted onto an ultrathin carbon grid (Agar Scientific). Chemical analysis is performed using  
85 Fourier transform infrared spectroscopy (FTIR) and X-ray photoelectron spectroscopy (XPS) core  
86 levels measurements. The FTIR is a Nicolet iS5 from Thermo Scientific equipped with an  
87 attenuated total reflectance (ATR) iD5 accessory. XPS and ultraviolet photoelectron spectroscopy  
88 (UPS) measurements were performed using an ESCALAB 250 Xi microprobe spectrometer  
89 (Thermo Fisher Scientific, UK), equipped with an X-ray and UV source. XPS analysis was carried  
90 out with a focused XR6 monochromatic, micro-focused  $\text{Al}_{K\alpha}$  ( $h\nu=1486.6$  eV,  $<900$   $\mu\text{m}$  spot sizes)  
91 radiation source with a hemispherical energy analyzer. The binding energy was calibrated against  
92 the  $\text{Pt}_{4f}$  peak taken to be located at 72.1 eV with a pass energy of 150 eV. XPS measurements  
93 were carried at a pressure  $1-5 \times 10^{-9}$  mbar. The valence band spectra were collected with a 20 eV  
94 pass energy. Optical absorption is obtained using a Perkin-Elmer 650S ultraviolet-visible (UV-  
95 Vis) spectrometer equipped with a 150 mm integrating sphere. For UV-Vis characterization, Si  
96 QDs were deposited on a quartz substrate forming a homogeneous film. For valence electron  
97 analysis XPS in the valence region, UPS and a Kelvin Probe were used. UPS spectra were  
98 collected with a UV source energy He(I) ( $h\nu = 21.22$  eV) at a pressure of approximately  $5.5 \times$   
99  $10^{-8}$  mbar, with 2 eV pass energy. A negative bias of 10 V was applied to the sample to shift the



100 spectra from the spectrometer threshold. The energy resolution was around  $\sim 100$  meV. The  
101 Kelvin probe (KP technologies APS04) is operated in atmosphere with a 2 mm gold alloy tip  
102 after calibrating the tip work function against a sputtered Au thin film ( $W_{\text{Au}} = 4.69 \pm 0.05$  eV,  $W_{\text{tip}}$   
103  $= 4.4 \pm 0.1$  eV). Additionally, the Kelvin probe (KP) setup is equipped with a surface photovoltage  
104 module which measures the surface contact potential difference (CPD) induced by a  
105 monochromated white light source and an air photoemission module (APS), which uses a  
106 deuterium lamp source ( $\Delta\lambda = 1$  nm) to induce photoemission of electrons from the samples. For  
107 XPS, UPS and KP samples are directly deposited to form a film of QDs on an ITO-coated glass  
108 (150 nm,  $15 \Omega/\text{sq}$ , VisionTek) in order to have good electrical contact with the stubs. The  
109 characterization of all the samples was carried out within 1 hour after the synthesis to limit the  
110 effect oxidation [26].

111

### 112 3. Results and Discussion

#### 113 3.1 Structural and chemical characterization

114 TEM results show that well-separated Si particles are produced for all values of precursor  
115 concentration introduced into the plasma (Figure S1 in supporting information). However, high  
116 resolution TEM (HR-TEM) images reveal major differences between the particles depending on  
117 the precursor concentration. In particular, high silane concentrations (150-200 ppm) lead to the  
118 production of amorphous particles, while with low concentrations (50 ppm) crystalline particles  
119 are obtained (Figure 1). As an example, figure 1a-b displays HR-TEM of a crystalline QD  
120 synthesized using a  $\text{SiH}_4$  concentration of 50 ppm and an amorphous QD produced with 200 ppm  
121 of the precursor, respectively. In Figure 1a, the particle exhibits fringes with spacing of 0.17 nm  
122 that corresponds to the (311) plane of the silicon crystalline lattice. More detailed evidence of the  
123 crystalline or amorphous character of the Si QDs is obtained using SAED. Figure 1c-d show  
124 SAED patterns for the two extreme conditions of precursor concentration considered (50 ppm and  
125 200 ppm). The crystallinity of the Si QDs produced using low  $\text{SiH}_4$  concentration, results in the  
126 observation of sharp spots that together form well-defined rings in the SAED pattern (figure 1c).  
127 The spots detected in the diffractogram match well with crystalline planes corresponding to the  
128 diamond lattice of silicon (see Figure S2 of the supporting information). On the other hand, a high  
129 concentration of precursor (150-200 ppm) results in faded diffuse rings in the SAED pattern that  
130 can be attributed to their amorphous character (Figure 1d). The conditions described above  
131 illustrate how our APP system is capable of producing highly crystalline QDs or purely  
132 amorphous QDs by controlling, in this case, the silicon precursor concentration. These results are  
133 in agreement with previous results published elsewhere [14, 16]. Hence, it is possible to adjust  
134 from crystalline Si QDs production with low precursor concentration in the plasma ( $\leq 50$  ppm),



135 to amorphous Si QDs with high concentrations ( $\geq 150$  ppm). For intermediate conditions the  
136 situation exhibits significant differences. TEM analysis of samples prepared using 100 ppm of  
137 SiH<sub>4</sub> concentration showed that within the particle size distribution, only the smallest ( $< 2$  nm)  
138 particles exhibited crystalline character, while larger particles were amorphous. Thus, at these  
139 conditions both crystalline and amorphous particles can be generated simultaneously. To further  
140 understand the mechanism that makes possible the crystallization process of QDs inside the  
141 plasma region, a collision-corrected model (CCM) has been used and the results are described  
142 below. Regarding the particle size analysis, low magnification TEM images have been used,  
143 counting over 500 QDs for each of the conditions. The TEM micrographs used for the calculations  
144 and the particle size histograms are included in figure S3 of the supporting information. The  
145 overall results are presented in figure 1e, showing the mean value and the standard deviation  
146 (these were obtained by fitting a log-normal distribution) of the QD size for various precursor  
147 concentrations, indicating the crystalline or amorphous character with red and blue color  
148 respectively. In the graph it is possible to observe that increasing the concentration of precursor  
149 in the plasma leads to the production of QDs with larger in size, with mean diameters varying  
150 from 1.7 nm to 3.6 nm. At the same time, the size dispersion also increases starting with a value  
151 of 0.6 nm for 50 ppm of SiH<sub>4</sub> and reaching a value of 1.8 nm for 200 ppm of SiH<sub>4</sub>.

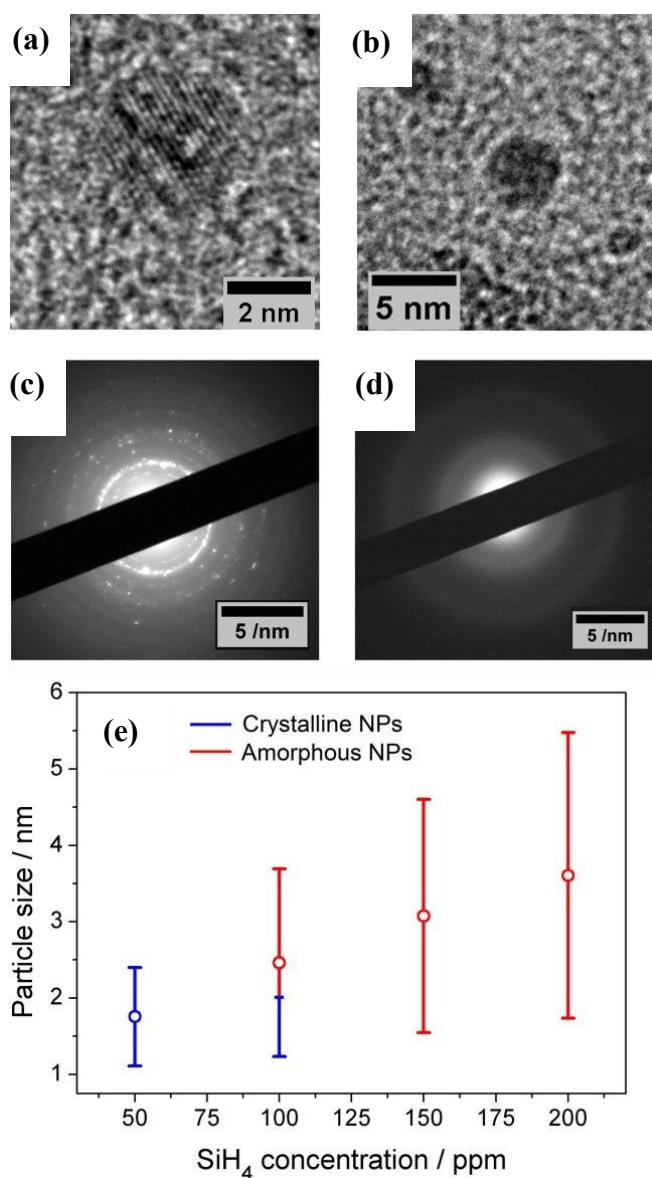
152 XPS technique has been used to characterize chemically the Si QDs produced for the different  
153 experimental conditions. The photoelectron spectra in the Si 2p region are shown in Figure 2a,  
154 along with a deconvolution of the peaks in the different oxidation states of Si. We can observe  
155 that only the crystalline samples show a higher binding energy shoulder which can be readily  
156 associated with limited oxidation. On the contrary, samples which have a least a fraction of  
157 amorphous particles do not show this feature.

158 Further details on the chemical composition of the Si QDs were produced by FTIR analysis.  
159 Figure 2b displays the FTIR spectra of Si QDs produced using the indicated SiH<sub>4</sub> concentration  
160 in the plasma. In the two selected regions of the infrared spectrum shown in figure 2b, it is possible  
161 to observe the vibrations that correspond to Si-O and Si-H<sub>x</sub> bonds. In particular, the absorption  
162 band at  $\sim 1075$  cm<sup>-1</sup> associated to Si-O-Si stretching modes is shown. This peak has very strong  
163 absorption cross section and therefore the low absorbance (lower than the Si-H<sub>x</sub> peaks) is evidence  
164 of a small level of oxidation even after exposure to atmosphere. Instead, the peaks at 783 cm<sup>-1</sup>,  
165 862 cm<sup>-1</sup>, 902 cm<sup>-1</sup> and 2139 cm<sup>-1</sup> are associated with the Si-H<sub>3</sub> bending, symmetric deformation,  
166 degenerate deformation and stretching mode, respectively [28,29]. The intensity of these peaks  
167 becomes significant for Si QDs synthesized using high precursor concentration (200 ppm) which  
168 correspond to amorphous samples, while it is negligible for lower concentrations when particles  
169 are crystalline. This suggests that when the synthesis is carried out using a silane concentration  
170 above 100 ppm, i.e. whenever some amorphous material is present, particles become partially  
171 hydrogenated possibly due to hydrogen incorporation within the QDs [16].

View Article Online  
DOI: 10.1039/C9FD00103D



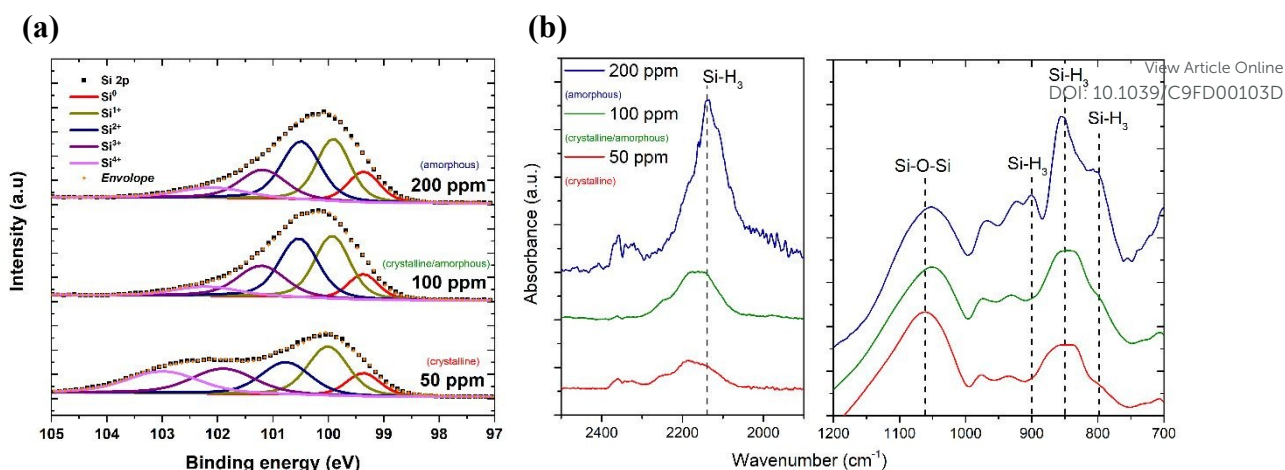
172

View Article Online  
DOI: 10.1039/C9FD00103D

173

174 **Figure 1.** Transmission electron microscopy (TEM) characterization of the Si quantum dots  
 175 (QDs). High resolution TEM of (a) a crystalline and (b) amorphous Si QD. (c) – (d) Selected area  
 176 electron diffraction (SAED) pattern of a) crystalline and b) amorphous Si QDs. (e) Mean particle  
 177 size (dots) and standard deviation (bars) of the Si QDs as a function of the precursor  
 178 concentration used; blue and red lines denote respectively the crystalline or amorphous character  
 179 of the QDs within the size distribution.





180

181 **Figure 2 – (a)** Deconvolution of XPS Si2p signal into components relative to the different  
 182 oxidation state of Si atoms, reflecting and increased amount of Si-O bonds with different  
 183 coordinations for the sample with crystalline nanoparticles. **(b)** Fourier transform infrared  
 184 (FTIR) spectra of Si QDs for the different precursor concentrations indicated. The dashed line  
 185 indicates vibrational transitions at 783 cm<sup>-1</sup>, 862 cm<sup>-1</sup>, 902 cm<sup>-1</sup> and 2139 cm<sup>-1</sup> wavenumbers and  
 186 are associated with the Si-H<sub>3</sub> bending, symmetric deformation, degenerate deformation and  
 187 stretching mode, respectively and a Si-O-Si absorption band at 1075 cm<sup>-1</sup>.

188

189 We already reported the stability of Si nanocrystals through FTIR measurements in a previous  
 190 study [26] over a period of 30 days and concluded that these nanocrystals, while being H-  
 191 terminated, tend to oxidize through a backbond oxidation process starting from water (e.g. from  
 192 humidity in air) condensation on the surface. However, this process is slow and self-limited  
 193 particularly when the QDs are deposited in films. Interestingly the amorphous particles seem to  
 194 be protected from oxidation at least in the first stages of exposure to atmosphere (<1 h) and within  
 195 the volume scoped by the XPS, a fact that could be ascribed to the different kinetics of oxidation  
 196 within amorphous particles [30,31] or due to the higher H concentration and the ability of  
 197 hydrogen to passivate dangling bonds more evenly than in the crystalline case. The degree of  
 198 hydrogenation therefore seems to be important both in the oxidation process as well as at some  
 199 level determining the phase of the QDs.

200 The XPS instrument also allows the acquisition of reflection electron energy loss spectra using  
 201 the flood gun as an electron source. This technique can be used to easily ascertain qualitatively  
 202 the presence of incorporated hydrogen within a sample, via an energy loss feature which sits  
 203 around 1.8 eV from the zero-loss peak. In our case we observe a (Figure S4, supporting  
 204 information) distinguishable peak for the conditions in which we obtain amorphous particles (100  
 205 ppm and 200 ppm) of SiH<sub>4</sub>. We believe that at these conditions the level of hydrogenation is  
 206 higher than in the other cases. When the QDs are crystalline (50 ppm) the presence of hydrogen  
 207 is limited at the surface and for this reason the hydrogen reflection signal is essentially absent.

208

### 3.2 Formation mechanisms leading to the synthesis of Si QDs



209 We used a model to calculate the temperature at the surface of the Si QDs ( $T_p$ ) during the  
210 synthesis process within the APP (see section S6 in Supporting Information). Figure 3 presents  
211 the estimated values of  $T_p$  corresponding to our synthesis conditions (black, red, green and blue  
212 squares); in the same graph we also plot the experimental crystallization temperature (CT, grey  
213 points) of Si QDs from the literature [32]. The CT divides the graph in two regions: particles with  
214 a temperature below the CT are expected to be amorphous (blue region in figure 3) while particles  
215 with a temperature above the CT are expected to present a crystalline character (orange region in  
216 Figure 3). Due to the intrinsic difficulty for measuring these values, it is not possible to define a  
217 sharp CT line to separate the two states [32]. Instead, a transition region represented by a white  
218 band can be defined (see Figure 3). It is possible to observe that for low SiH<sub>4</sub> concentrations (50  
219 ppm, black squares) the data points are all located entirely on the crystalline side of the graph.  
220 This result clearly agrees with the experimental evidence reported in figure 1, that is, the  
221 formation of purely crystalline Si QDs. For high precursor concentrations (> 100 ppm) the  
222 opposite situation is observed. In this case,  $T_p$  is mainly located in the amorphous region with  
223 only the smallest, and less numerous, particles near the crystallization band. This is again in  
224 agreement with experimental data of Figure 1, where amorphous particles were observed for these  
225 conditions. The inability to produce a sufficiently high QD temperature for the crystallization of  
226 the Si QDs under these conditions can be partly attributed to the lower energetic plasma conditions  
227 (see Figure S5) but also to the larger particle size produced. At intermediate SiH<sub>4</sub> flow (100 ppm),  
228 only the smallest particles are located on the crystalline side and the rest lay on the crystallization  
229 band as indeed confirmed in our QDs characterization (Figure 1). These results provide theoretical  
230 justification to the experimental observations since only particles smaller than 2 nm were found  
231 to be crystalline for this intermediate condition.

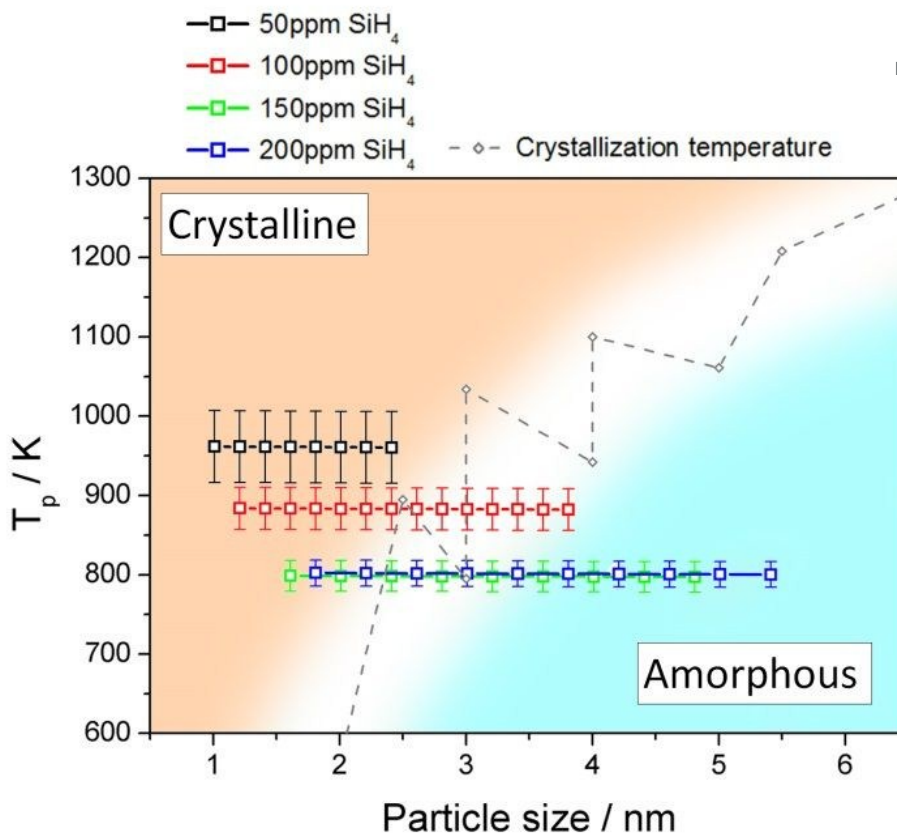
### 232 3.3 Valence band, Fermi level and bandgap measurements

233 The functional properties of semiconductors, in particular for energy applications, depend on  
234 the electronic structure and how the energy band parameters align with other application device  
235 components. We therefore perform here the experimental evaluation of energy band diagram  
236 (EBD) parameters such as valence/conduction band edges, Fermi level and bandgap for our  
237 samples. All measurements are therefore conducted on films of QDs deposited on solid substrates.  
238 Firstly, we focus on the valence band maximum (VBM) and Fermi level; in the next section we  
239 will complement these results with bandgap measurements to produce the EBD of both crystalline  
240 and amorphous QDs. To evaluate the electron energy levels near the valence band region and  
241 Fermi levels, we combined and compared results from different measurement techniques which  
242 offer different features, whose results are reported in Table 1.

View Article Online  
DOI: 10.1039/C9FD00103D

Faraday Discussions Accepted Manuscript





243 **Figure 3.** Particle temperature calculated using the collision-corrected model (CCM) for the  
 244 different concentration of precursor introduced in the plasma and experimental crystallization  
 245 temperature from reference [32]. The temperature has been calculated for the particle size  
 246 distribution obtained for each condition. The crystallization temperature divides the graph in  
 247 crystalline (orange) and amorphous (blue) regions.

248

Sample	Fermi Level / eV		VBM / eV			Eg / eV
	$E_{F-Kp}$	$E_{F-UPS}$	$VBM_{UPS}$	$VBM_{XPS}$	$VBM_{APS}$	$E_{g-UVVIS}$
50 ppm	- 6.0 ± 0.1	- 4.7 ± 0.1	-5.9 ± 0.1	-6.3 ± 0.6	-5.7 ± 0.2	2.47 ± 0.07
100 ppm	- 4.0 ± 0.1	- 4.3 ± 0.1	-6.2 ± 0.1	-6.4 ± 0.6	-6.1 ± 0.2	2.6 ± 0.1
200 ppm	- 3.9 ± 0.1	- 3.5 ± 0.1	-5.7 ± 0.1	-5.8 ± 0.6	-5.8 ± 0.3	2.3 ± 0.1

249

250 **Table 1** - Fermi levels determined from Kelvin probe ( $E_{F-Kp}$ ) and UPS ( $E_{F-UPS}$ ) measurements with  
 251 corresponding errors. For the Kelvin probe measurement, the error corresponds to std. deviation  
 252 measurements within the scoped area and for the UPS measurement it is mostly due to the  
 253 spectrometer energy resolution. VBM values determined from UPS ( $VBM_{UPS}$ ) and APS ( $VBM_{APS}$ )  
 254 with corresponding errors are also reported.  $VBM_{XPS}$  was calculated from XPS measurements  
 255 and the Fermi levels produced by UPS. Errors correspond to energy resolution for UPS and XPS,  
 256 and for APS a rms sum of std. deviation relative to the fit. Energy bandgaps obtained through  
 257 Tauc plots of transmittance and reflectance measurements, assuming an indirect bandgap  
 258 functional dependence between absorption coefficient and light energy. Errors are a rms sum of  
 259 errors from fitting and uncertainty due to the light source instabilities.

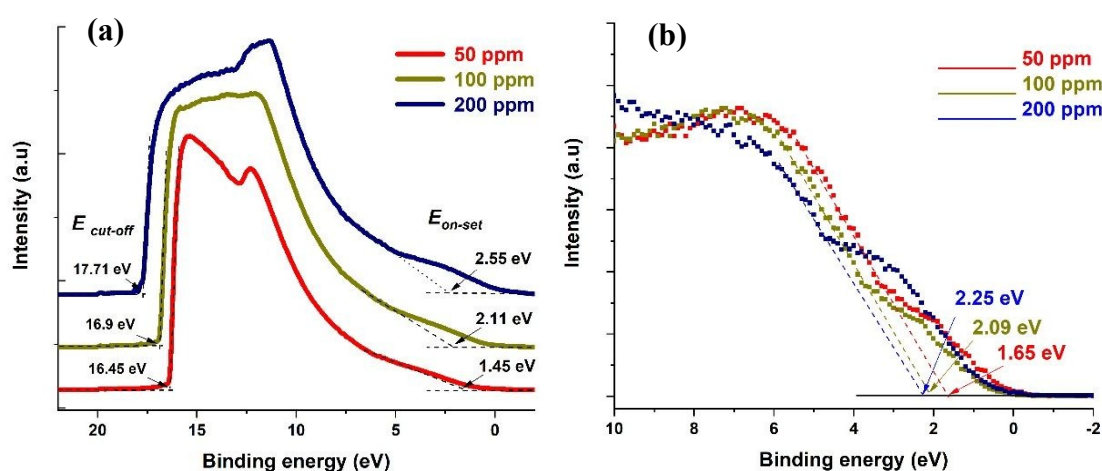


260 UPS can be used to obtain the absolute value of the Fermi Level of a semiconductor as well as  
 261 the VBM. UPS measurements produce a cut-off energy ( $E_{cut-off}$ ) and an on-set energy ( $E_{on-set}$ )  
 262 which relate to the binding energy of electrons originating from the deepest levels of the material  
 263 (ionized by the He-I source,  $h\nu = 21.22$  eV) and from the valence band region, respectively (Figure  
 264 4a). We should note that the UPS signal is referenced to the Fermi level of the semiconductor  
 265 material under analysis. Therefore, the Fermi level can be extracted from the difference between  
 266  $E_{cut-off}$  and the energy of the He-I photons, i.e.  $E_{F-UPS} = E_{cut-off} - 21.22$  eV (see Table 1). The VBM  
 267 is calculated also from the UPS measurements where  $VBM_{UPS} = E_{F-UPS} - E_{on-set}$  (Table 1).

268 Fermi level values obtained with the Kelvin Probe show the same trend as the ones obtained by  
 269 UPS, even though the values are different, and in one case (50 ppm) particularly higher.

270 Meanwhile XPS produces the difference between the Fermi level and the VBM (Figure 4b). In  
 271 order to determine the values of the VBM reported in Table 1, we have used the Fermi levels  
 272 obtained by UPS (also in Table 1). Finally, the APS technique is similar in principle to the lower  
 273 energy range of the UPS, but it is operated in atmosphere and the source is a deuterium lamp,  
 274 which is not able to reach a cut-off in the photoemitted electrons. From the APS signal it is  
 275 possible to extract an absolute value of VBM (See supporting information section S9).

276



277 **Figure 4** – (a) UPS spectra for the three different samples showing both cut-off and on-set values.  
 278 (b) XPS valence band spectra showing the difference between VBM and Fermi level.

279

280 All the values summarized in Table 1 are also reported in Figure 5. The comparison shows that  
 281 discrepancies from different measurements do exist, which in most cases are within measurement  
 282 errors. Differences even above 0.1 eV can be significant for applications, however we should note  
 283 that the literature seldomly reports a comparison of different measurement techniques and as such  
 284 our results highlight and underline the difficulties and limitations of current and available  
 285 measurement methods.



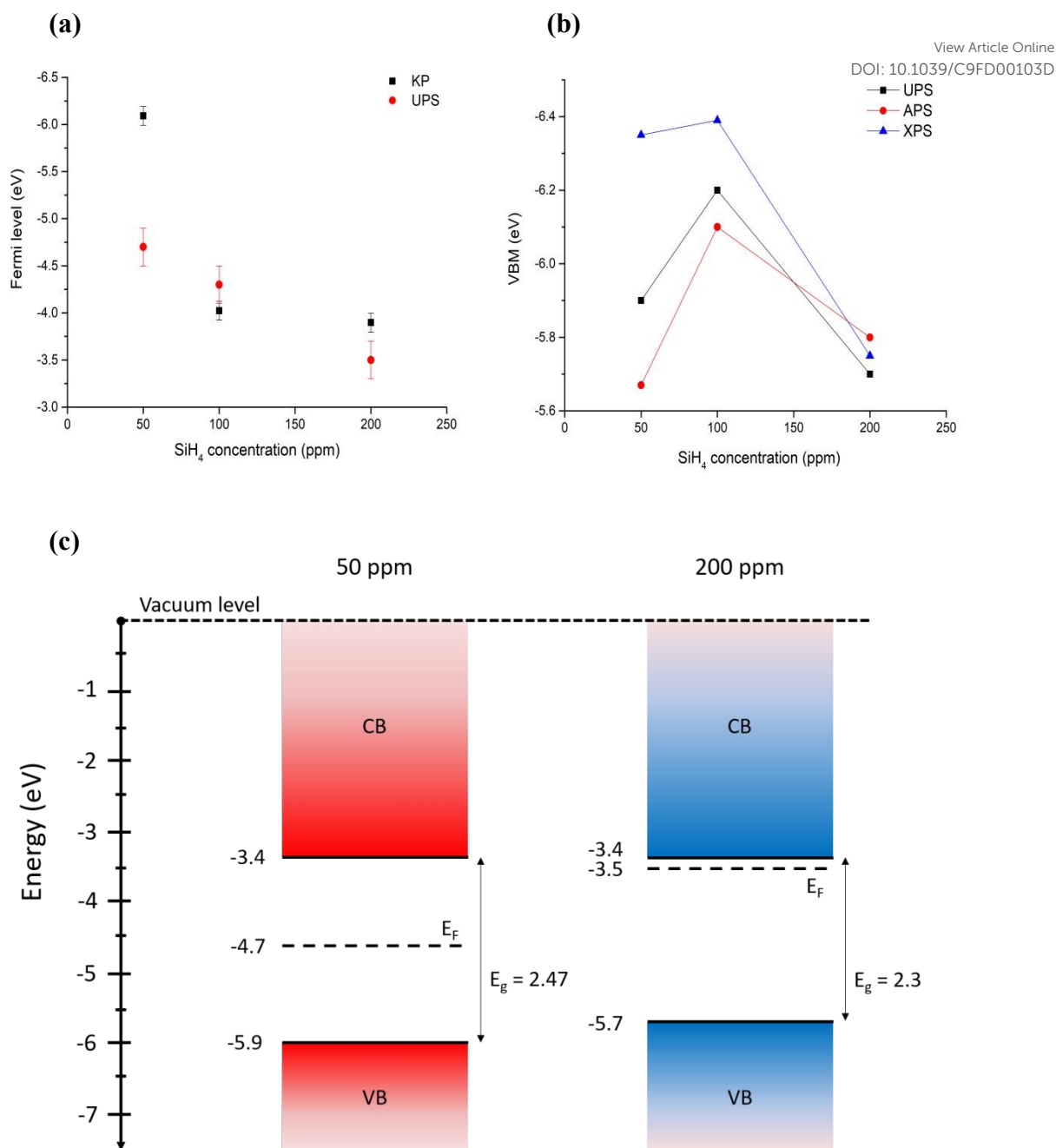
286 With the exception for one of the measurements, the Fermi levels show similar values and  
287 exhibit the same trend, i.e. the Fermi energy becoming smaller with the particles going from  
288 crystalline to amorphous (Figure 5a). The value of the Fermi level for the crystalline QDs (50  
289 ppm) stands out and emphasizes the strong surface sensitivity of the KP technique (1-3  
290 monolayers); while stray capacitance originating from inhomogeneities in the film can also  
291 impact the measurement, we tentatively ascribe this very large value of the Fermi level to the  
292 impact of even minor surface oxidation. The VBM values also show similar trends (Figure 5b)  
293 with differences that can be justified by measurement errors, with the exception of the VBM  
294 values of crystalline QDs (50 ppm) measured by XPS, which may be due to difficulties in  
295 extracting a good and reliable fit to the x-axis due to the limited resolution. A critical evaluation  
296 of the capabilities of each technique is therefore needed in order to choose which approach is  
297 most suitable and reliable in this specific case.

298 UPS measurements are implicitly limited by the general mechanism involved in the  
299 photoemission as the light interacting with the sample induces a surface dipole which complicate  
300 the evaluation of the Fermi level and VBM values, especially in conductive or highly doped  
301 samples [33]. In our case we assume that our samples are not developing a particularly strong  
302 surface dipole, since we do not expect the samples to be highly conductive. However, the UPS  
303 signal strength rely on the high photoemission yield, the narrow energy resolution achievable and  
304 the ability to scope only the occupied electron states of the very top surface of a solid (2-3 nm).  
305 Instead XPS in the valence band region suffers from moderate energy resolution, lower yields and  
306 the absence of an energy cut-off which does not permit to obtain values relative to the vacuum  
307 level and generally scopes a “deeper” region beneath the surface (5-10 nm) [34]. Both techniques  
308 though are operated in high vacuum, which can help preserving the state of surfaces.

309 KP and associated APS operated in atmosphere are instead subject to surface dipoles and  
310 surface chemistry induced by environmental adsorbates which can easily shift the values up to  
311 few eV raising or lowering the barriers felt by electrons escaping the material or even induce  
312 completely new energy levels, especially in the valence electrons region. These may be  
313 considered as systematic errors in the values, which cannot be accounted for if there is not a  
314 rigorous knowledge of the surface chemistry. While they are mostly useful for characterizing  
315 surfaces which will be exposed to atmosphere (e.g. for corrosion studies) they also have  
316 advantages of being cheap, easy and fast techniques. In addition, KP measurements are not  
317 affected by light-induced dipoles. However, APS operates in atmosphere and photoelectrons  
318 experience different electrostatic environment as higher or lower potential barriers when escaping  
319 from the material's surface.

320





321

322 **Figure 5 – (a)** Comparison of Fermi level measured with Kelvin Probe and UPS. **(b)** Comparison  
 323 of VBM values measured (UPS, APS) and calculated (XPS) with different techniques, error bars  
 324 are omitted for clarity and can be found in table 1. **(c)** Energy band diagrams obtained combining  
 325 UPS values for Fermi level and VBM, and energy bandgaps through Tauc plots for the extreme  
 326 cases 50 ppm and 200 ppm of Silane, which correspond to the smallest ( $\langle r \rangle = 1.8$  nm) all  
 327 crystalline particles and the biggest ( $\langle r \rangle = 3.6$  nm) all-amorphous ones.

328

329 These conditions depend on the atmospheric species and can change substantially with ambient  
 330 temperature and humidity. In other words, while UPS and XPS are referenced to a potential  
 331 energy of the ultra-high vacuum in the XPS chamber, the APS values are referenced to the



332 electrostatic potential at the atmospheric conditions at the time of measurements [35]. It is clear  
333 that various techniques can be used for the determination of VBM and Fermi levels, however care  
334 should be taken in the selection of the most appropriate technique.

335 UV-Vis transmission and reflectance spectra were acquired for Si QDs. In all the cases, Si QDs  
336 exhibit continuous and relatively featureless optical characteristics. Transmission and reflectance  
337 measurements can be used to determine the bandgap of the Si QDs. A full description of the  
338 bandgap determination can be found in the supporting information (section S7), which were  
339 calculated using Tauc plots with a 1/2 coefficient corresponding to an indirect bandgap [36]. A  
340 similar argument holds for amorphous silicon particles, for which the joint optical density of states  
341 is modeled by a square law [37,38]. For low precursor concentrations (50 ppm), QDs present a  
342 bandgap of roughly 2.5 eV (see Table 1) and as previously observed (Figure 1e) these  
343 experimental conditions generate crystalline particles. This value is consistent with H-terminated  
344 Si-QDs in the size range reported (1.8 nm). However, for SiH<sub>4</sub> concentrations greater than 100  
345 ppm, value at which we start to observe amorphous particles (Figure 1e), the bandgap (more  
346 rigorously mobility gap) tends to a value of about 2.3-2.5 eV, which is consistent with the  
347 expected value for amorphous Si [39]. The bulk bandgap of amorphous silicon is reported in the  
348 wide range 1.6-1.97 eV, a condition that strongly depends on the content of hydrogen and on the  
349 degree of structural disorder introducing or relieving stress components. The relative importance  
350 of the two mechanisms is still debated [40-42]. The higher values in respect to bulk counterparts  
351 may be ascribed to quantum confinement effects, given the small particle size that we obtained.  
352 This fact could be explained by an increased content of hydrogen which has been found with the  
353 REELS spectrum (Figure S4 in supporting information). The 200 ppm Silane samples, which  
354 resulted in the biggest amorphous-only particles, additionally shows a long absorption tail to sub-  
355 bandgap energies that may be due to unsaturated bonds, ultimately acting as shallow dopant  
356 levels.

357 The surface photovoltage module in the KP can detect small amounts of photoinduced charge  
358 on a sample surface. The ability to build charge on the surface depends both on the light-induced  
359 bending of energy levels due to surface states, that results either in charge accumulation or  
360 depletion, and charge carriers mobilities [43]. We observe a detectable photovoltage only in the  
361 samples with amorphous particles (see Figure S8 in supporting information). The threshold in  
362 energy for the appearance of a photovoltage shows similar values as optical gaps (2.3 eV to 2.5  
363 eV) found via UV-Vis absorption, and the sign of the shift indicates that samples have an n-type  
364 behavior. This implies that charge transport within the layer of amorphous particles may be  
365 superior in respect to the films of crystalline nanoparticles [43].

### 366 3.3 Energy level diagram



367 Based on our discussion in section 3.2, we can expect XPS and APS to be somewhat less  
368 accurate for the determination of the VBM. The former because of a lower counts and resolution  
369 at lower energies which tend to overestimate the difference between VBM and Fermi level, given  
370 the inability to resolve weaker signals. The latter is susceptible to environmental conditions and  
371 adsorbates at a higher degree than the other techniques. For the same reason, Fermi level through  
372 Kelvin Probe may be equally dependent on the calibration value, which is obtained by the APS  
373 method and may be affected by ambient temperature, humidity and by adsorbates on the particle's  
374 surface.

375 We believe in conclusion that UPS values are more reliable both for the determination of  
376 absolute Fermi level and for the VBM, under the only assumption of negligible light-induced  
377 surface dipole. Using energy bandgap values from UV-Vis spectroscopy and UPS values, we  
378 have produced the energy band diagram of our single-phase samples (Figure 5c).

379 The result is that, while valence band maxima and bandgap do not vary significantly with the  
380 crystalline state of our nanoparticles, the value of Fermi level tend to get closer to the conduction  
381 band edge with increased amounts of amorphous particles giving a stronger n-type character to  
382 the films. The UV-Vis longer wavelength (sub-gap) absorption and the photovoltage response of  
383 amorphous samples do support this picture.

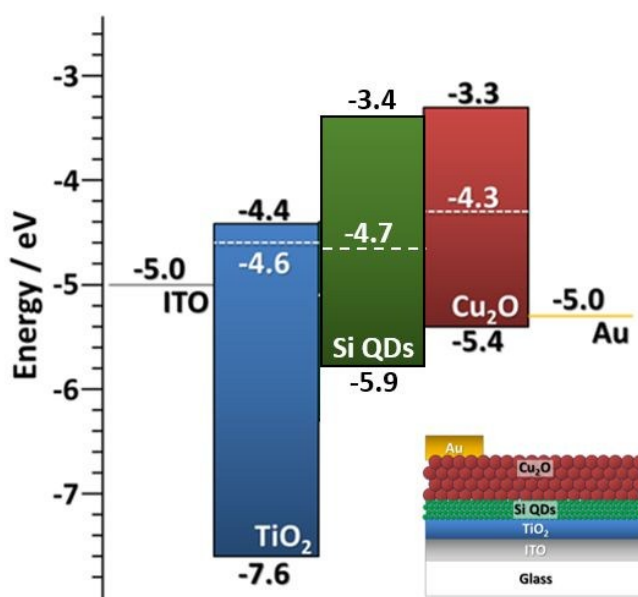
#### 384 **4. Application as active layers in PV cells**

385 In this section we finally provide some details on the integration of Si QDs in photovoltaic (PV)  
386 devices. This is mainly to show that a better knowledge of the EBD parameters can benefit the  
387 application development and also in part to demonstrate the capability of the APP process for  
388 direct integration of QDs in experimental devices. We have evaluated the performance of all-  
389 inorganic PV cells using the crystalline Si QDs synthesized with our method (50 ppm). The  
390 particles are directly deposited as a homogeneous film with the help of a two-axis stage placed 1  
391 cm below the exit orifice of the capillary. Two device architectures were explored, both having  
392 Si QDs as the active component for the photogeneration of electron-hole pairs (see also  
393 Supporting Information).

394 One of the device architectures is illustrated in figure 6a, the other in supporting information  
395 S10. We used indium-doped tin oxide (ITO) strip-coated glass (VisionTek Systems Ltd., 15  $\Omega$ /sq,  
396 150 nm ITO thickness) as our substrate and transparent conductive contact. A TiO<sub>2</sub> layer (40 nm  
397 thick) is formed using a sol-gel method and spin-coating following the protocol previously  
398 described [44] on top of the transparent conductive substrate. The TiO<sub>2</sub> coated ITO-glass is then  
399 used as a substrate to directly deposit the Si QDs (3  $\mu$ m thick film) exiting from the plasma reactor,  
400 using an X-Y stage to ameliorate the uniformity of the deposited layer. Spray-deposited Cu<sub>2</sub>O is  
401 then used as an electron blocking layer and a sputter-deposited gold film is used as a top contact.



402 The non-equilibrated band diagram of the cell is shown in figure 6. We should note that the  
 403 selection of the  $\text{Cu}_2\text{O}$  transport layer was informed from our EBD measurements. The  
 404 performance of the device was assessed with a solar simulator (Sub Femtoamp Keithley 6430) at  
 405 standard AM1.5 irradiation. Open-circuit voltage and fill factor of 0.785 V and 87% were  
 406 obtained, respectively. These are remarkable figures of merit that we can partly ascribe to  
 407 exceptional good energy level alignment of the Si QDs with the selected transport layer and  
 408 contacts; however, the current density is very poor and is affecting the overall performance.  
 409 Additionally, the measured value of series resistance is also indicative of relatively efficient  
 410 electron transport in the cell (table S10 in supporting information). Our current set-up could not  
 411 deliver thinner Si QDs films as normally employed in this type of devices; a reduction of the  
 412 thickness can contribute to some improvements in the current density and overall device  
 413 performance.



416 **Figure 6.** Non-equilibrated band diagram for the PV device based on Si QDs as active layers,  
 417  $\text{Cu}_2\text{O}$  QDs as electron blocking layer, a  $\text{TiO}_2$  film hole blocking layer and corresponding contacts.  
 418 Inset, diagram of the layer structure of the relative device.

419  
 420 While the overall performance remains very low, the device parameters are very encouraging  
 421 and demonstrate the usefulness of a careful EBD parameters analysis. The utilization of both  
 422 amorphous and crystalline Si QDs for PVs remains debatable and recent trends show that further  
 423 manipulation through surface modification, alloying or other methodologies will be required  
 424 [45,46]. In this context, the feasibility and integration of APP processes in the fabrication of next  
 425 generation devices is very promising and can result advantageous.



426

427

## 428 5. Conclusions

429

430 We have demonstrated that Si QDs with tunable crystallinity can be grown in APPs. The study  
431 of a variety of experimental conditions has enabled us to produce Si QDs exhibiting crystalline  
432 or amorphous characteristics. The crystalline or amorphous character of the Si QDs was  
433 explained by the efficient heating of the particles in non-thermal APPs. The analysis of the energy  
434 balance on the surface of the particles shows that the plasma parameters can be tuned to control  
435 the temperature of the particles when immersed in the plasma and hence, their crystallinity. We  
436 built an electron energy diagram of the valence electrons regions for two selected samples, one  
437 with completely crystalline nanoparticles and one with completely amorphous nanoparticles and,  
438 after a critical assessment of measurements from different instruments, found that films formed  
439 from these free-standing particles tend to develop an n-type character for charge carrier in  
440 amorphous nanoparticles, despite similar values of valence band edges and optical bandgaps. We  
441 also showed the potential of APP processes for the fabrication of all-inorganic PV cells. Our  
442 analysis also highlights the need for improving analytical techniques and methodologies so that  
443 could be used more extensively to dictate application-focused research directions.

444

## 445 Acknowledgements

446 This work was supported by the EPSRC (EP/K022237/1, EP/M024938/1, EP/R008841/1) and the  
447 Leverhulme International Network (IN-2012-136).

448

## 449 References

- 450 [1] Priolo F, Gregorkiewicz T, Galli M and Krauss TF 2014 *Nat. Nanotechnol.* **9**, 19-32  
451 [2] Mastronardi ML, Henderson EJ, Puzzo DP and Ozin GA 2012 *Adv. Mater.* **24**, 5890-5898  
452 [3] Kim DK, Lai Y, Diroll BT, Murray CB and Kagan CR 2012 *Nat. Commun.* **3**, 1216  
453 [4] Park J, Gu L, von Maltzahn G, Ruoslahti E, Bhatia SN and Sailor MJ 2009 *Nat. Mater.* **8**,  
454 331-336  
455 [5] Švrček V, Mariotti D, Shibata Y and Kondo M 2010 *J. Phys. D: Appl. Phys.* **43**, 415402-  
456 415410  
457 [6] Mariotti D, Mitra S and Švrček V 2013 *Nanoscale* **5**, 1385-1398  
458 [7] Švrček V, Kondo M, Kalia K and Mariotti D 2009 *Chem. Phys. Lett.* **478**, 224-229.  
459 [8] Švrček V, Mariotti D and Kondo M 2010 *Appl. Phys. Lett.* **97**, 161502



- 460 [9] Wolf O Dasog M, Yang Z, Balberg I, Veinot JGC and Millo O 2013 *Nano Lett.* **13**, 2516-  
461 2521
- 462 [10] Dasog M, De los Reyes GB, Titova LV, Hegmann FA and Veinot JGC 2014 *ACS Nano* **8**,  
463 9636-9648.
- 464 [11] Kusova K *et al* 2010 *ACS Nano* **4**, 4495-4502
- 465 [12] Švrček V, Dohnalova K, Mariotti D, Trinh MT, Limpens R, Mitra S, Gregorkiewicz T,  
466 Matsubara K and Kondo M 2013 *Adv. Funct. Mater.* **23**, 6051-6058
- 467 [13] Sagar DM, Atkin JM, Palomaki PKB, Neale NR, Blackburn JL, Johnson JC, Nozik AJ,  
468 Raschke MB and Beard MC 2015 *Nano Lett.* **15**, 1511-1516
- 469 [14] Askari S, Levchenko I, Ostrikov K, Maguire KP and Mariotti D 2014 *Appl. Phys. Lett.* **104**,  
470 163103
- 471 [15] Askari S, Macias-Montero M, Velusamy T, Maguire P, Svrcek V and Mariotti D, 2015, *J.*  
472 *Phys. D: Appl. Phys.* **48**, 314002
- 473 [16] Askari S, Svrcek V, Maguire P and Mariotti D, 2015, *Adv. Mater.*, **27**, 8011–8016
- 474 [17] Anthony R and Kortshagen U, 2009, *Phys. Rev. B* **80**, 115407
- 475 [18] Shen Z, Kortshagen U, and Campbell SA, 2004, *J. Appl. Phys.* **96**, 2204
- 476 [19] Street RA 1981 *Adv. Phys.* **30**, 593-676
- 477 [20] Kortshagen U, 2009, *J. Phys. D: Appl. Phys.* **42** 113001
- 478 [21] Kortshagen U, Mangolini L, Bapat A, 2006 *Nanotechnology and Occupational Health*, 39-  
479 52
- 480 [22] Mangolini L, Thimsen E, and Kortshagen U, 2005, *Nano Lett.*, **5** (4), pp 655–659
- 481 [23] Gresback R, Holman Z, and Kortshagen U, 2007, *Appl. Phys. Lett.* **91**, 093119
- 482 [24] Mariotti, D.; Sankaran, R. M. Perspectives on atmospheric-pressure plasmas for  
483 nanofabrication, 2011 *J. Phys. D: Appl. Phys.*, **44**, 174023
- 484 [25] Wagner AJ, Mariotti D, Yurchenko KJ and Das TK 2009 *Phys. Rev. E* **80**, 065401.
- 485 [26] Macias-Montero M, Askari S, Mitra S, Rocks C, Ni C, Svrcek V, Connor PA, Maguire P,  
486 Irvine JTS and Mariotti D. 2016 *Nanoscale* **8**, 6623-6628
- 487 [27] Askari S, Macias-Montero M, Velusamy T, Maguire P, Svrcek V and Mariotti D, 2015, *J.*  
488 *Phys. D: Appl. Phys.* **48**, 314002
- 489 [28] Tautz F.S and Schaefer JA 1998 *J. Appl. Phys.* **84**, 6636-6643.
- 490 [29] Chabal YJ 1991 *Physica B* **170**, 447-456
- 491 [30] Z.H. Lu, E. Sacher and A. Yelo, 1988 *Philosophical Magazine B*
- 492 [31] A. Szekeres, P. Danesh, 1995, *Journal of Non-Crystalline Solids* **187**
- 493 [32] Goldstein AN 1996 *Appl. Phys. A* **62**, 33-37
- 494 [33] M.M. Beerbom, B. Lagel, 2006 *Journal of Electron Spectroscopy and Related Phenomena*  
495 **152**

View Article Online

DOI: 10.1039/C9FD00103D



- 496 [34] S. Hüfner, *Photoelectron Spectroscopy: Principles and Applications*, 2013, Springer Science  
497 & Business Media
- 498 [35] A. Kahn, 2016, *Materials Horizons* **1**
- 499 [36] Tauc J 1968 *Mater. Res. Bull.* **3**, 37-46
- 500 [37] N. F. Mott, E.A. Davis, *Electronic Processes in Non-Crystalline Materials*, 1971  
501 Clarendon-Press, Oxford
- 502 [38] M L Theye, 1989, *Physica Scripta*
- 503 [39] N.-M. Park, T.-S. Kim, and S.-J. Park, 2001, *Appl. Phys. Lett.*, **78**, 17
- 504 [40] Abdulraheem Y, Gordon I, Bearda T, Meddeb H and Poortmans J, 2014, *AIP Advances* **4**,  
505 057122
- 506 [41] A.M. Berntsen and W. F. van der Weg, 1993, *physical review B*
- 507 [42] G. D. Cody, T. Tiedje, B. Abeles, B. Brooks, and Y. Goldstein, 1981, *Phys. Rev. Lett.* **47**,  
508 1480
- 509 [43] L. Kronik, Y. Shapira, 1999, *Surface Science Reports*, **37**
- 510 [44] Carolan D, Rocks C, Padmanaban DB, Maguire P, Svrcek V and Mariotti D  
511 2017, *Sustainable Energy Fuels*, 2017, **1**, 1611-1619
- 512 [45] V. Švrček, D. Mariotti, R.A. Blackley, W.Z. Zhou, T. Nagai, K. Matsubara and M. Kondo,  
513 2013, *Nanoscale*, **5**, 6725-6730
- 514 [46] M. Bürkle, M. Lozac'h, C. McDonald, D. Mariotti, K. Matsubara, and V. Švrček, 2017, *Adv.*  
515 *Funct. Mater.*, **27**, 1701898

View Article Online  
DOI: 10.1039/C9FD00103D

